Defect Limitations in $Cu_2ZnSn(S,Se)_4$ Solar Cells Utilising an In_2S_3 Buffer Layer

Stephen Campbell,[1] Yongtao Qu,[1] James Gibbon,[2] Holly J. Edwards,[2] Vin R. Dhanak,[2] Devendra Tiwari,[1] Vincent Barrioz,[1] Neil S. Beattie,[1] and Guillaume Zoppi[1, a)]

[1)] *Department of Mathematics, Physics and Electrical Engineering, Ellison Building, Northumbria University, Newcastle upon Tyne, NE1 8ST, UK.*

[2)] *Stephenson Institute for Renewable Energy, University of Liverpool, Liverpool L69 7ZF, UK.*

(Dated: April 27, 2020)

Currently, kesterite $Cu_2ZnSn(S,Se)_4$ (CZTSSe) device architecture incorporates a CdS *n*-type buffer which is non-ideal due to the presence of toxic Cd. Other buffers such as In_2S_3 have been proposed as an alternative. In this study, optical and electronic characterisation techniques together with device analysis and simulation were used to assess nanoparticle-based CZTSSe absorbers and solar cells with CdS and In_2S_3 buffers. Photoluminescence spectroscopy indicated CZTSSe absorbers with In_2S_3 buffer had a lower density of detrimental non-radiative defects and a higher concentration of copper vacancies $V_{Cu}{}^{+}$, responsible for *p*-type conductivity in CZTSSe, in comparison to the absorber with CdS buffer. Capacitance-voltage (*C-V*) measurements revealed the In_2S_3 buffer-based CZTSSe devices had a three times higher apparent doping density and a consequently narrower space charge region than devices with a CdS layer. This resulted in poorer collection of photo-generated charge carriers in the near-IR region despite a more favourable band alignment as determined by X-ray photoelectron and inverse photoelectron spectroscopy. The presence of interfacial defect states in In_2S_3 devices as determined by *C-V* and biased quantum efficiency measurements are also responsible for the loss in open-circuit voltage compared with reference devices with CdS.

I. Introduction

Chalcopyrite photovoltaic (PV) materials, such as $Cu(In,Ga)(S,Se)_2$ (CIGSSe), were developed as absorber layers in thin film solar cell (TFSC) technology to proffer an alternative to market-dominant silicon PV. The limited supply of compositional elements In and Ga in CIGSSe has directed research efforts towards finding more abundant elemental substitutions, with structurally similar kesterite $Cu_2ZnSn(S,Se)_4$ (CZTSSe) being identified as a promising alternative PV compound. Of all the fabrication processes available[1–9], CZTSSe thin film absorbers synthesised from nanoparticle inks offer a low cost solution-based processing method for large scale printed roll-to-roll application. The current record power conversion efficiency (PCE) of 12.6% for CZTSSe-based solar cells[10] was achieved in 2013, whereas counterpart CIGSSe-based devices achieved efficiencies up to 22.9%[11]. The large disparity in performance between kesterite and chalcopyrite PV devices is primarily attributed to a severe open circuit voltage (V_{oc}) deficit of about 600 mV in CZTSSe solar cells compared to values around 400 mV in CIGSSe devices[10,12].

Several reasons for the V_{oc} deficit have been cited: i) high densities of intrinsic defects in the kesterite bulk, such as vacancies (e.g. V_{Zn}, V_{Sn}), antisites (e.g. Sn_{Cu}, Sn_{Zn}) and interstitials (e.g. Zn_i) which act as effective electron-hole recombination centres[13], ii) band tailing which is also related to high concentrations of defects in conjunction with a high degree of charge compensation causing electrostatic potential fluctuations[14–16] or heterogeneous spatial variations in crystallinity and/or composition leading to nanoscale bandgap fluctuations[17–19] and iii) enhanced buffer/absorber interface recombination due to non-optimal band alignment depending on buffer selection[14,20,21].

A suitable strategy to reduce the V_{oc} deficit in kesterite-based solar cells is the investigation of band alignments at the buffer/absorber interface to facilitate selection of suitable *n*-type buffer materials with an optimal conduction band offset (CBO). The CBO is most relevant in the conjunction of *n*-type buffer with *p*-type absorbers, where the minority charge carriers are electrons. In this instance, electrons are promoted to the conduction band (CB) of the *p*-type absorber and optimum device performance is governed by efficient transport of electrons across the interface into the *n*-type buffer for onward extraction from the device.

Band alignment at semiconductor interfaces can be categorised as Type I, II or III, however Type III are not pertinent to PV applications. In Type I, the CB of the absorber is lower than that of the buffer (relative to the electron vacuum levels of the materials) forming a spike-like potential barrier which can hinder electron transport dependent on the magnitude of the CBO. A theoretical optimal value of 0.4 eV for the spike-like offset has previously been reported in CZTSSe[22]. If the CBO is below this threshold electron transport is facilitated by tunnelling and/or thermionic emission. A small 'spike' CBO has been shown to create an absorber type inversion in the vicinity of the heterojunction which consequently creates a large hole barrier[23]. In contrast, the CB of the absorber layer at a Type II interface is higher than that of the buffer layer forming a cliff-like alignment. Although there is no barrier for electrons to overcome when flowing from absorber to buffer, there may be high concentrations of holes near the semiconductor junction increasing the probability of interface recombination[23,24]. Therefore, Type I and II CBO are preferable in order to achieve improvements in V_{oc} and short circuit current density J_{sc}, respectively.

[a)] Corresponding author: guillaume.zoppi@northumbria.ac.uk

In kesterite solar cells, CdS is used ubiquitously as the *n*-type material in device architecture despite the buffer having a slightly larger than optimal CBO with CZTSSe which can lead to enhanced interface recombination[25,26]. As an alternative, In_2S_3 has been considered due to the material having a more favourable CB alignment with CZTSSe and a large energy bandgap[27,28]. In fact, Jiang *et al* successfully incorporated a thin In_2S_3 layer in a CZTS-based device achieving an efficiency of 6.9%[29] and Mitzi *et al*. demonstrated CZTSSe devices with lowest V_{oc} deficit by applying a double In_2S_3/CdS emitter[30].

In this study we aim to demonstrate how replacing the conventional CdS buffer with In_2S_3 in CZTSSe device architecture can potentially lead to an improvement in V_{oc}. First, we determine the nature of the CBO at the buffer/absorber heterojunction using X-ray photoemission (XPS) and inverse photoemission (IPES) spectroscopy to ascertain which material forms a more favourable band alignment with CZTSSe absorbers fabricated from nanoparticle inks. We then investigate whether the deposition method of the buffer layer can affect changes in the chemical and electronic properties of the absorber material in the region near the interface. To this end, temperature and excitation dependent photoluminescence (PL) measurements of as-deposited, CdS- and In_2S_3-buffered CZTSSe thin films are conducted to elucidate details of the main recombination mechanism present in the absorbers and associated shallow defects which contribute towards such recombination. By applying a number of electrical characterisation techniques, quantitative demonstration is made on how the application of different buffers impacts device performance. Furthermore, device modelling using solar cell capacitance simulations (SCAPS) was done to gain an insight on the relationship between CdS/CZTSSe and In_2S_3/CZTSSe interface defects and device performance.

II. Experimental details

A typical substrate solar cell configuration was used in this study, i.e. glass/Mo/CZTSSe/buffer (In_2S_3 or CdS)/*i*-ZnO/indium tin oxide (ITO)/Ni-Al. CZTSSe films were prepared from CZTS nanoparticle inks. Firstly, CZTS nanoparticles were fabricated using a well-established hot-injection method following our previously published procedure[31,32]. The resulting nanoparticle inks were then deposited on molybdenum substrates via spin coating to form the CZTS precursor thin film with a thickness of $\sim$1 μm. Thereupon, CZTS precursor thin films were annealed in a selenium atmosphere to introduce grain growth, resulting in CZTSSe absorbers[33]. The resulting CZTSSe thin films had the following composition; Cu (at%): 20.25 $\pm$0.32, Zn: 11.95 $\pm$0.60, Sn: 11.75 $\pm$0.24, S: 2.90 $\pm$0.55, Se: 53.15 $\pm$1.41 and metallic ratios Zn/Sn: 1.02, Cu/(Zn+Sn): 0.85. Buffer layers of CdS ($\sim$60 nm) and In_2S_3 ($\sim$70 nm) were prepared by chemical bath deposition (CBD). Specifically, cadmium sulphate, thiourea and ammonium hydroxide were mixed in a glass reactor for CdS deposition with details given elsewhere[34]. In terms of In_2S_3 deposition, samples were immersed in a solution composed of indium chloride (10 mM), thioactamide (0.1 M) and acetic acid (0.1 M) at 70 °C to form an In_2S_3 coating on CZTSSe[29,35]. After the deposition, the samples were removed from the bath, rinsed with deionized water and dried under a nitrogen stream. The buffer coated samples were then annealed at 200 °C in open air for different times, i.e. CdS for 10 min and In_2S_3 for 2 min. The transparent oxide layers, including *i*-ZnO ($\sim$35 nm) and ITO ($\sim$200 nm) layers were then deposited by magnetron sputtering. Front contact grids which are composed of Ni ($\sim$50 nm) and Al ($\sim$1 μm) layers were deposited through a shadow mask by electron beam evaporation. Finally, nine $\sim$0.16 cm^2 cells were defined by mechanical scribing on each substrate.

XPS measurements were performed in a standard UHV chamber, which had a base pressure <2 x10^{-10} mbar, the main residual gas of which was hydrogen. A monochromatic Al Kα SPECS XR 50 M source ($h\nu$ = 1486.6 eV) operating at a nominal power of 250 W was used in conjunction with a PSP Vacuum Technology Ltd Resolve 120 MCD5 electron energy analyzer. The calibration of the spectrometer was performed by aligning the Ag 3d$_{5/2}$ and Fermi level to their known energy positions of a clean polycrystalline Ag foil. By fitting the Fermi-Dirac distribution to the Ag Fermi level, the experimental resolution of the analyzer is found to be 0.37 $\pm$0.05 eV. The measured spectra are charge-corrected to the C 1s peak at 285.00 eV, due to adsorbed, adventitious carbon. The spectra were analysed using the CasaXPS software. Core-levels were fitted with pseudo-Voigt functions atop a Shirley background. Valence band maxima (VBM) positions were found by linear extrapolation to the background. The errors on core-level binding energies and the VBM were determined to be $\pm$0.05 eV. IPES were performed in the same chamber using a PSP Vacuum Technology BaO cathode dispenser electron source and an isochromat NaCl photon detector, both of which were at 45° to the sample normal. The lowest unoccupied molecular orbital of a thick C_{60} multilayer, deposited in situ, was used to calibrate the photoemission spectra. The spectrometer resolution was determined to be 1.00 $\pm$0.10 eV from fitting the Fermi level of a clean, polycrystalline Ag foil. To obtain the interfacial samples, a PSP Vacuum Ltd ISIS 3000 ion source was used to Ar^+ ion (E_k=0.25 keV) etch material away from the sample with an ion flux of 6.25 x10^{13} ions cm^{-2}s^{-1} until the interface was visible in XPS measurements. This typically corresponds to an overlayer thickness of 2-3 nm.

PL spectra were measured using a Horiba Jobin Yvon fully automated spectrometer fitted with an InGaAs PMT detector cooled to -30 °C to reduce noise. A 532 nm continuous wave diode-pumped solid state (CW-DPSS) laser was used as an excitation source. Low temperature PL measurements were performed by placing the samples in a Janis SHI-4-2 closed cycle refrigeration cryostat using compressed He gas coupled with a Lakeshore Model 355 temperature controller. All PL measurements were performed on selenised absorber layers deposited on Mo coated glass. For temperature-dependent PL measurements a relatively low laser power of $\sim$100 mW/cm^2 was selected to avoid excessive heating of the CZTSSe films.

Current density-voltage (*J-V*) parameters of completed

CZTSSe devices were extracted using an Abet Technologies solar simulator at 1-sun (100 mW/cm^2) illumination. Capacitance-voltage (*C-V*) and capacitance-frequency (*C-f*) measurements were performed using an Agilent E4980a LCR meter and Ametek VersaSTAT 3 potentiostat/galvanostat, respectively. External quantum efficiency (EQE) measurements were performed using a Bentham PVE300 system calibrated using a combined Si/InGaAs photodiode. A Shimadzu UV-2600 spectrophotometer was used to obtain transmittance/reflectance data for CdS, In_2S_3 and CZTSSe films on soda-lime glass (SLG).

III. Results and discussion

A. Band alignment at buffer/CZTSSe interface

The Kraut method is frequently used to experimentally determine the band alignments at semiconductor interfaces[36–38]. This method uses the photoelectron spectra of a series of three samples to determine the band offsets at an interface, namely a thick overlayer sample (buffer), a substrate sample (CZTSSe) and an interfacial sample in which the core-levels from both the substrate and the overlayer (buffer/CZTSSe) are visible. By determining the relative energy positions of the core-levels ($E_{cl}^{over,sub}$) to the VBM (ξ_{VBM}^{sub}) and the difference in energies of the core-levels in the interfacial sample, the valence band offset (ΔE_v) can be determined by

$$\Delta E_v = (E_{cl}^{over} - \xi_{VBM}^{over}) - (E_{cl}^{sub} - \xi_{VBM}^{sub}) - (E_{cl}^{over} - E_{cl}^{sub}) \quad (1)$$

The bandgaps of the semiconductors are given by $E_g^{over,sub} = \xi_{VBM}^{over,sub} + \xi_{CBM}^{over,sub}$, thus the CBO ($\Delta E_c$) can be derived from

$$\Delta E_c = E_g^{over} - E_g^{sub} - \Delta E_v \quad (2)$$

In order to determine the band alignment at the CdS/CZTSSe and In_2S_3/CZTSSe interfaces, the valence band offset (VBO) and CBO are measured for individual 3d core levels in Cd, In, Sn and Se and 2p core levels in S, Cu and Zn and the final VBO and CBO for the semiconductor interfaces is obtained from the mean of the individual core level values (experimental core level values are listed in Supp. Table S1) . Figures 1a, c, and e show the determination of the VBM as measured by XPS and 1b, d, and f show the CBM as measured by IPES for CdS, In_2S_3 and CZTSSe films, respectively. Note that the spectra show states tailing into the band gap, which is an artefact of instrumental broadening and not a measure of defect states, see Supp. Fig. S1. Using the aforementioned method, VBO values of ΔE_v = -1.98 $\pm$ 0.10 eV and -1.21 $\pm$ 0.10 eV and CBO values of ΔE_c = -0.68 $\pm$ 0.14 eV and 0.39 $\pm$ 0.14 eV were determined for CdS and In_2S_3 buffered samples, respectively. The calculated band alignment for each sample are represented schematically in Fig. 2a. It is apparent CdS forms a large cliff-like CBO (Type II) at the heterojunction with CZTSSe (greater than other reported values[25,39,40]) whereas In_2S_3 forms a modest spike-like CBO (Type I). Device simulation has shown that the ideal CBO is a moderate spike in the range 0 – 0.4 eV[41–43]. However, as the experimentally determined CdS/CZTSSe CBO is -0.68 eV, this cliff barrier inhibits the flow of injected electrons from buffer to absorber under forward bias conditions causing an accumulation of electrons at the interface. Charge carrier recombination is therefore elevated at the heterojunction and V_{oc} is reduced as a consequence[42]. Also, Scheer demonstrated the activation energy of interface recombination in a generic heterojunction PV device is equivalent to the energy difference between the CBM of the buffer and VBM of the absorber layers[24]. Thus, with regard to interface recombination, a cliff-like CBO will result in a lower activation energy than the absorber bandgap leading to a reduction in V_{oc}. The spike-like CBO of +0.39 eV at the *pn*-junction of the In_2S_3-buffered CZTSSe sample is almost at the threshold for efficient electron transport across the buffer/absorber interface (0.4 eV[22]). Notwithstanding the magnitude of the spike offset in this sample, interface recombination is still expected to be reduced due to a limited supply of holes at the junction caused by absorber type inversion[23]. Band alignment can also influence the degree of quasi Fermi level splitting at the heterojunction under illumination, depicted schematically by the dashed lines in Fig. 2a. V_{oc} is enhanced by the spike-like CBO at the In_2S_3/CZTSSe interface in comparison to cliff-like offset at the CdS/CZTSSe junction. Based on XPS and IPES measurements of nanoparticle-derived CZTSSe device-like stacks, In_2S_3 is a more appropriate buffer material to enhance device V_{oc} than conventional CdS. Furthermore, SCAPS simulations on CdS- and In_2S_3-buffered CZTSSe devices were performed using the XPS/IPES data, see Fig. 2b. It is clearly evident the 'spike' CBO in the In_2S_3 based device translates to a significant improvement in V_{oc} compared to the device with CdS buffer.

B. Photoluminescence measurements

In order to rule out the existence of possible binary and ternary compounds, Raman spectroscopy was performed to investigate the crystal quality of as-deposited CZTSSe reference, CdS- and In_2S_3 buffered CZTSSe absorbers fabricated from the same batch of nanoparticle inks, see Supp. Figure S2. The two sharp peaks at 173 and 197 cm^{-1} correspond to CZTSe[44]. All three CZTSSe thin films have a high quality kesterite crystal structure with no obvious secondary phases observed.

To determine whether the deposition of different buffers causes any modification to the surface region of CZTSSe films, low temperature excitation intensity PL measurements were made on the CZTSSe films. As the absorption coefficient α of CZTSSe is $\sim$4 x10^4 cm^{-1} for the laser excitation wavelength of 532 nm, it can be assumed the incident laser light is fully absorbed within the first 250 nm of the CZTSSe absorber in all three samples[45]. The results of the excitation dependent PL of all CZTSSe samples at 6 K are presented in Fig. 3. PL spectra for all samples exhibit a broad asymmetric shape where the shallower low energy slope is related to the joint density of states (JDOS) of CB/VB tails[46–48] and the steeper high energy slope depends on the photogenerated carrier distribution[17], see Fig. 3a. The asymmetric nature of the PL bands is indicative of a semiconductor with a high degree of band tailing due to spatial fluctuations of VB and/or CB edges[49]. The os-

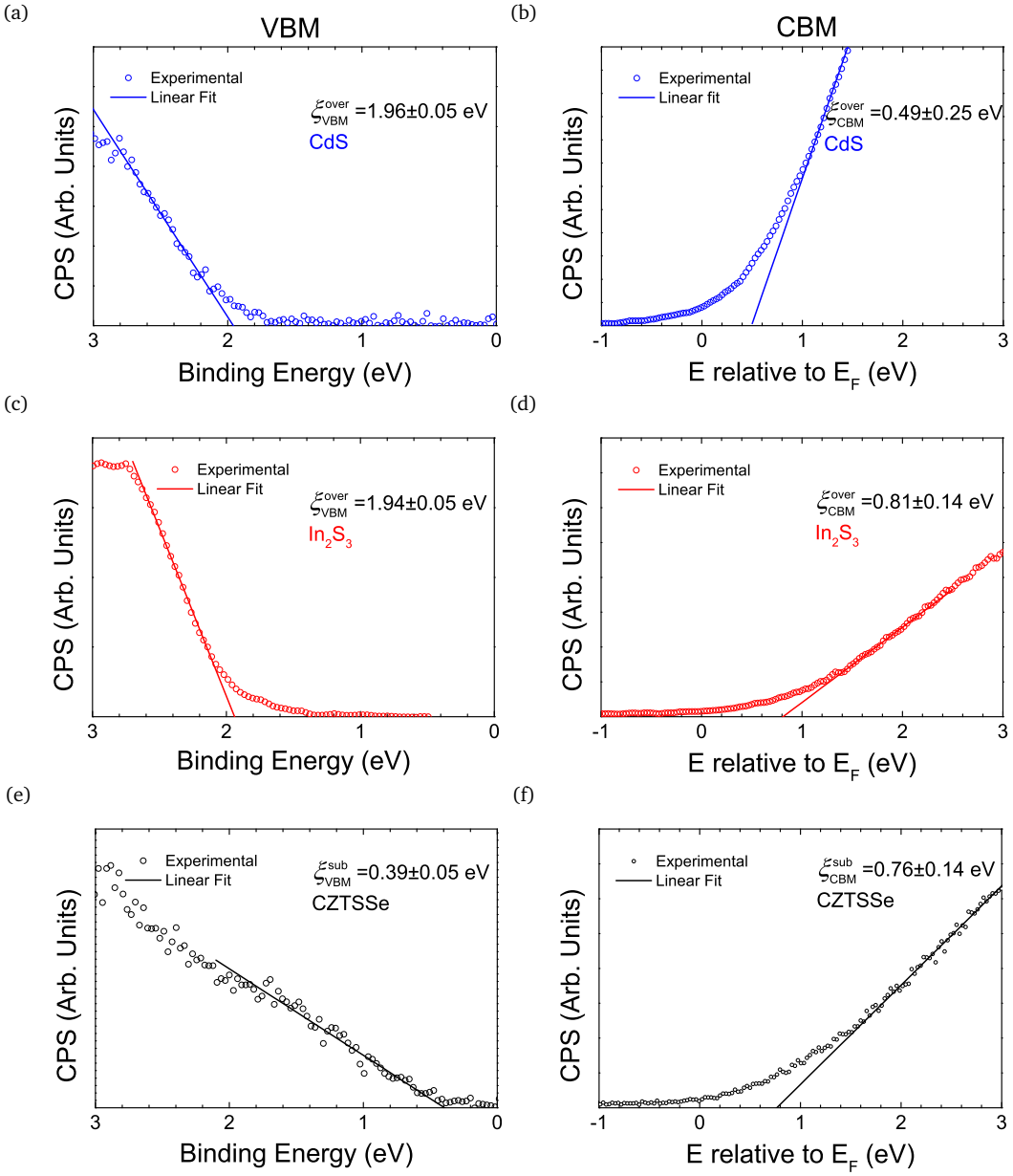

FIG. 1. Valence band maximum regions as measured by XPS for thick samples of (a) CdS, (c) In_2S_3 and (e) CZTSSe and conduction band minimum as measured by IPES for the same samples (b) CdS, (d) In_2S_3 and (f) CZTSSe. Combining XPS/IPES data gives estimated bandgaps of 2.45, 2.75 and 1.15 eV for CdS, In_2S_3 and CZTSSe, respectively. These values are in good agreement with bandgap values of 2.42, 2.72 and 1.14 eV determined from UV-VIS measurements, respectively.

cillations around 0.9 eV are due to water vapour absorption. For all samples, the PL peak maxima exhibit strong blue-shifts with increasing excitation intensity up to a saturation point with no increase in PL intensity or peak shift upon higher excitation. An indication of the radiative process is given by evaluating the so-called k value which can be determined from the power law relation between the integrated PL intensity and excitation power, $I_{PL} \propto P^{k}$[50]. Values of $k > 1$ are expected for band-related recombination whereas $k < 1$ indicates defect-mediated recombination. Fig. 3c shows a log-log plot of the dependence of I_{PL} on P for all CZTSSe absorber samples, where k can be evaluated from the gradient of a straight fit to the data. The k values for all samples are less than unity (k-Ref = 0.76 ± 0.04, k-CdS = 0.81 ± 0.03 and k-In_2S_3 = 0.80 ± 0.04) suggesting the main recombination mechanism is related to defects within the bandgap of the absorber and remains unchanged regardless of buffer deposition. The presence of charge carriers localised at defects with energy levels above (below) the VB (CB) is further indicated by the strong blue-shift of PL peak maxima with increasing excitation intensity. The blue-shifting PL energy maxima for CZTSSe samples as a function of increasing laser power are shown in Fig. 3b. The energetic shift parameter β has a similar value of ∼14 meV/decade for the as-deposited reference and In_2S_3 buffered absorbers increas-

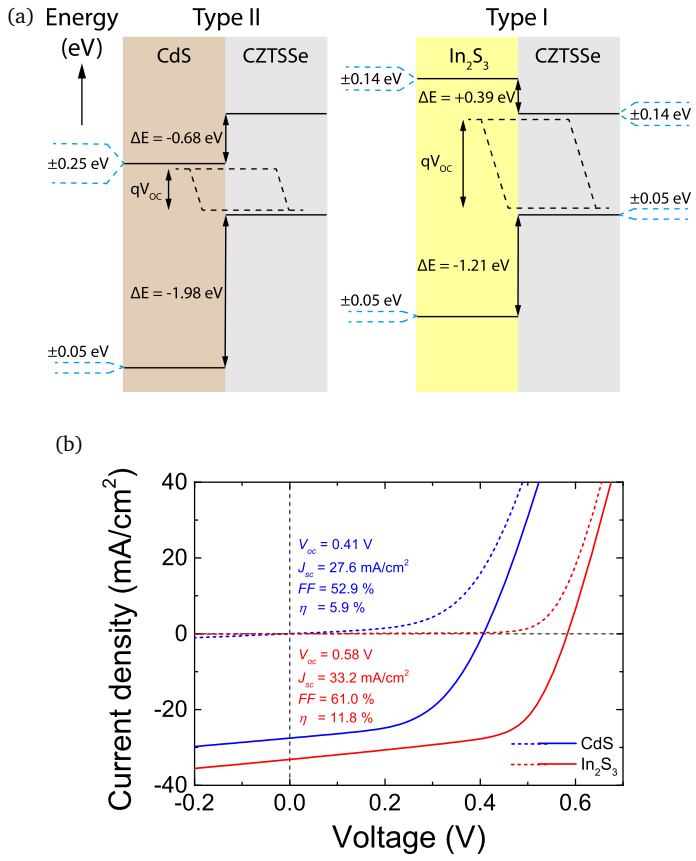

FIG. 2. (a) Experimentally determined band alignment from XPS/IPES data for CdS/CZTSSe (left) and In_2S_3/CZTSSe (right) interfaces. A small 'spike' in the conduction band offset at the In_2S_3/CZTSSe interface theoretically increases V_{oc} compared to that of a 'cliff' alignment at the CdS/CZTSSe interface. The dashed lines represent the degree of quasi fermi level splitting at the buffer/absorber interface and (b) SCAPS device modelling showing increased V_{oc} in In_2S_3-buffered CZTSSe device related to better band alignment. The dashed lines are *J-V* measurements in the dark and solid lines under 1-Sun illumination. Data for the CZTSSe has been derived from experiments on nanoparticle absorbers.

ing to ∼18 meV/decade for the CdS sample. The increase in β value for CdS-buffered absorber indicates a higher degree of charge compensation than the other CZTSSe based films[46].

Here radiative recombination can be explained by different models: i) quasi donor-acceptor (QDAP) and ii) spatial electrostatic potential fluctuations[51–55]. The QDAP model is used to describe radiative recombination in strongly compensated semiconductors where the DAP model is modified to account for the interaction between clusters of charged acceptor and donor defects. Similarly, electrostatic potential fluctuations are characterised by a constant bandgap with parallel shifts in the VB and CB edges due to spatial variations in concentration of charged defects, creating potential wells in the VB and CB. The presence of both electrostatic potential fluctuations and bandgap fluctuations are also expected to some degree in highly doped and compensated kesterites such as CZTSSe with Cu-Zn disorder in the crystal lattice. Bandgap fluctuations are changes in the material bandgap at the nanoscale caused by compositional inhomogeneities[17,18,56].

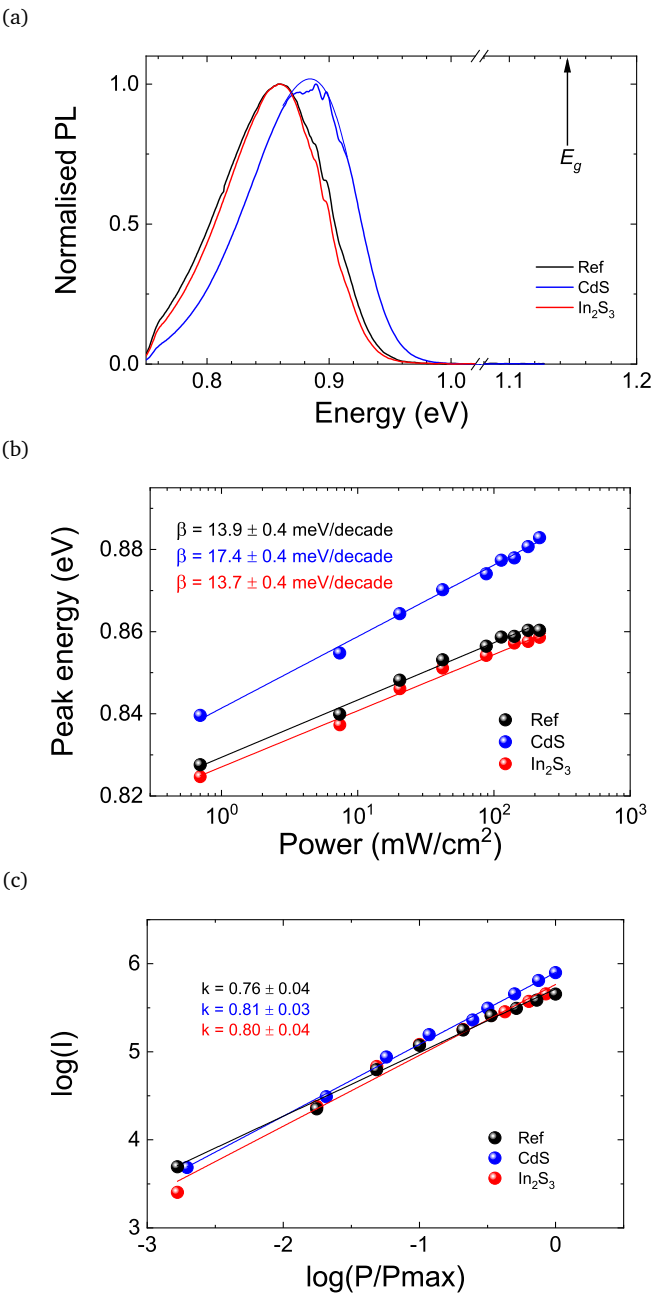

FIG. 3. (a) Normalised 6 K PL spectra of all films excited with same laser intensity showing significant shift of PL peaks from estimated room temperature bandgap of ∼1.14 eV (the oscillations around 0.9 eV are due to water vapor absorption, the thin blue line is asymmetric double sigmoidal fit to PL spectra), (b) evolution of PL band maxima with increasing P and (c) derivation of k parameter from $I \approx P^k$.

In considering the energetic blue-shift of PL peak maxima with increasing excitation intensity, Zacks and Halperin conclude the expected β values for the QDAP model should only be ∼8(2) meV/decade for CZTS(CZTSe)[57]. In comparison, the β values determined

for all types of CZTSSe film studied here are significantly higher, which would indicate the observed excitation dependent behaviour is also influenced by electrostatic potential fluctuations. Here increasing numbers of photogenerated carriers due to increasing excitation intensity screen the Coulomb potential of the charged defects, consequently flattening the band edge fluctuations. Thus the average depth of these potential fluctuations γ reduces as the excitation intensity increases (the potential fluctuation depth γ will be discussed in more detail later). Electrostatic potential fluctuations give rise to a number of radiative transitions, such as tail-to-impurity (TI) where electrons trapped in CB tail states recombine with holes localised at acceptor levels and exhibit similar behaviour to QDAP at low temperatures[54].

The higher degree of charge compensation in the buffered samples could be attributed to the diffusion of elements such as In and Cd across the buffer/absorber interface during buffer deposition forming additional acceptor and donor defects in the absorber near the heterojunction. Alternatively, the deposition of a buffer layer could act to passivate the CZTSSe film surface by reducing the number of non-radiative defect centres. The large β value determined for the CdS-buffered sample would suggest higher concentrations of self-compensated defect cluster in the CZTSSe material. The CZTSSe absorbers in all thin film samples studied here are non-stoichiometric, grown in a Cu poor and Zn rich environment. Under such conditions, the concentrations of self-compensated defect clusters [V_{Cu} + Zn_{Cu}] and [Zn_{Sn} + 2Zn_{Cu}] are expected to be high[26]. The observed increase in compensation in the absorbers with buffer layers (albeit slight in the case of In_2S_3) could be accounted for by the formation of additional antisite defects such as Cd_{Cu} and In_{Sn} promoted by buffer deposition conditions[29,58–63]. Due to the valencies of Cd and In atoms, antisites Cd_{Cu} and In_{Sn} form donor and acceptor defects, respectively. In the case of Cd_{Cu}, high concentrations in the top region of CZTSSe would contribute to *n*-type doping effectively reducing the overall *p*-type doping density, increasing charge compensation and enlarging the depletion region. Conversely, *p*-type doping would rise in the interface region of CZTSSe absorber due to acceptor state In_{Sn}. It has also been reported by several groups that Cu diffuses from the CZTSSe absorber into the CdS as a result of an annealing step following buffer deposition[60,64,65].

The resulting rise in density of V_{Cu} point defects can further increase the Cu depletion and *p*-type doping of the CZTSSe surface region. The effect of buffer deposition on apparent doping density will be discussed later (doping and depletion region width from *C-V* profiling and effects of interface defects from *C-f* measurements). PL spectra were fitted with asymmetric double sigmoidal function (DSF) proposed in[47] so as to determine the position of the PL peak maximum. The PL peaks of the as-deposited reference and In_2S_3-buffered films are coincidental and red-shifted by ∼30 meV compared to the CdS-buffered film. This suggests the CdS deposition conditions modify the absorber structure near the interface. Yan *et al*. investigated the effect of a 300 °C post-deposition heat treatment on CdS/Cu_2ZnSnS_4 (CZTS) heterojunction and found an interdiffusion of Cd and Zn between the buffer and absorber with diffusion depths of 200 and 15 nm for Cd and Zn, respectively[59]. High-angle annular dark-field (HAADF) imaging confirmed the presence of Cd_{Cu} antisite defects in the top region of the CZTS film. It is also possible for Cd to occupy Zn sites forming alloy $Cu_2Cd_xZn_{1-x}SnS_4$ (CCZTS) with a different bandgap to the bulk material. Both observations could account for the shift in PL peak position illustrated in Fig. 3a.

The average depth of band edge potential fluctuations γ is directly proportional to the total charged defect density N_t (which includes both radiative and non-radiative defects)[52,53,66]. Siebentritt *et al*. determined the low energy tail in PL spectra $I_{PL}(E)$ followed a Gaussian distribution which accurately described the defect-related nature of absorption tails caused by electrostatic potential and/or bandgap fluctuations such that

$$I_{PL}(E) \sim exp\left(-\frac{(E-E_0)^2}{2\gamma^2}\right) \quad (3)$$

where E_0 is the average emission energy with respect to fluctuating potentials[48]. Values for γ can be readily deduced from examination of PL emission bands and the absorber total defect concentration N_t subsequently determined. The maximum value of γ occurs when all QDAP states are fully occupied, i.e. maximum Coulombic attraction between defect clusters. Hence γ values of 54.8 ± 0.1, 55.0 ± 0.1 and 56.8 ± 0.1 meV were determined for as-deposited reference, In_2S_3-buffered and CdS-buffered absorbers, respectively. The increase in γ for the CdS-buffered sample could be ascribed to an increase in charge compensation. For a highly compensated *p*-type material with a fixed acceptor density such as CZTSSe, $\gamma \propto N_t$ (where N_t is the sum of charged acceptor $N_A{}^+$ and donor $N_D{}^-$ concentrations and $N_A \approx N_D$), therefore an increase in donor concentration N_D will result in an increase in potential fluctuation depth γ. In this case, the total number of ionised defects increases together with the level of compensation which in turn reduces the number of free holes. The screening length of charge carriers is thereby reduced which also contributes to an increase in γ.

The results of temperature-dependent PL measurements are presented in Figs. 4 and 5. Here PL spectra were obtained using laser excitation intensity just below the saturation of PL peak energy to ensure emission stems from QDAP/TI recombination alone (and not from additional contributions due to band-related recombination, see Supp. Fig. S4). In Fig. 4, the PL signal for the as-deposited film is fully quenched at temperatures greater than 160 K which suggests carriers are efficiently redistributed into non-radiative states. The appearance of a PL peak around 0.96 eV as temperature rises to 300 K in CdS- and In_2S_3-buffered films indicates another radiative recombination mechanism becomes predominant. The evolution of PL peak maxima with increasing temperature for all films is illustrated in Fig. 5a. The PL peak in the as-deposited film shows a slight red-shift in temperature range 6 - 60 K before exhibiting a slight blue-shift as tem-

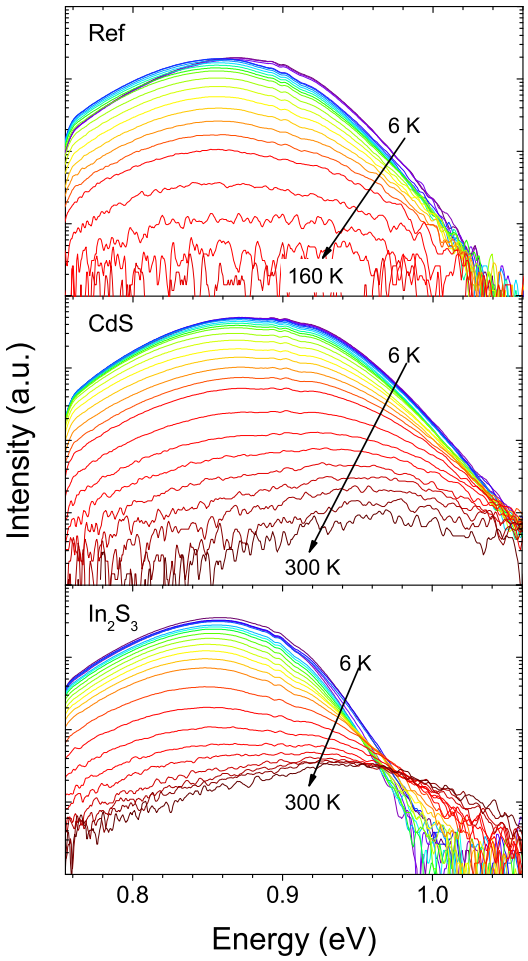

FIG. 4. Temperature dependence of PL spectra for as-deposited reference, CdS- and In_2S_3-buffered CZTSSe films at laser power P = 1.7 W/cm^2.

perature is increased up to 160 K, whereupon PL emission is thermally quenched. The buffered films demonstrate a different behaviour. Both buffered films show a red-shift of the band maximum at a greater rate than the as-deposited film as temperature rises from 6 K. The PL peaks of both films then blue-shift significantly at temperatures higher than T_{min} = 60 K and 100 K for CdS-buffered and In_2S_3-buffered samples, respectively. Similar QDAP behaviour was observed for CZTSSe solid solutions[64,67,68].

Further analysis of the temperature dependence of PL spectra reveals the activation energies of defects involved in the recombination mechanisms for the studied films. A two-defect model (Fig. 5b) best describes the observed thermal quenching:

$$I_{PL}(T) = \frac{I_0}{1 + c_1 exp\left(-\frac{E_{a1}}{kT}\right) + c_2 exp\left(-\frac{E_{a2}}{kT}\right)} \quad (4)$$

where I_0 is the integrated PL intensity extrapolated to 0 K, c_1 and c_2 are process rate parameters and E_{a1} (for $T < T_{min}$) and E_{a2} (for $T > T_{min}$) are the defect activation energies. The determined activation energies E_{a1} and E_{a2} are 14 $\pm$ 1, 12 $\pm$ 1, 7 $\pm$ 1 meV and 62 $\pm$ 8, 55 $\pm$ 3, 46 $\pm$ 7 meV for as-deposited reference, CdS-buffered and In_2S_3-buffered films, respectively. Previous studies have attributed the shallow level E_{a1} to the CB average potential well depth rather than a discrete defect level based on temperature-dependent PL peak behaviour for $T < T_{min}$[64,67].

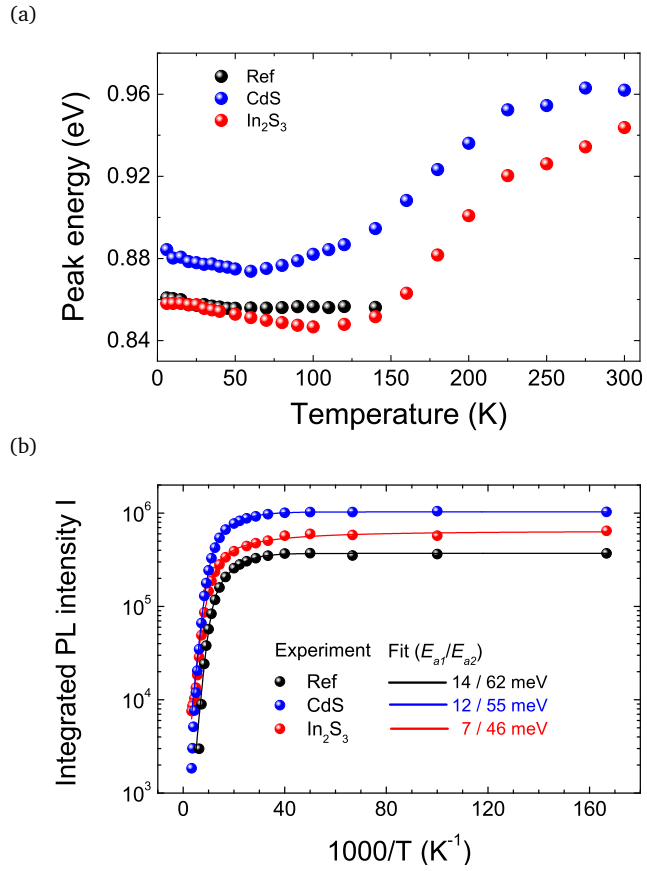

FIG. 5. (a) Maximum PL peak position vs. temperature showing a change in recombination mechanism with increasing temperature and (b) Arrhenius plot of integrated PL with derived defect activation energies.

Activation energy E_{a2} is associated with radiative recombination in the temperature regime $T_{min} < T <$ 295 K. Given the similarity in γ and E_{a2} values for all three CZTSSe films, it would be reasonable to assume radiative transitions involve tail states as T approaches room temperature. However, in a compensated material the PL peak is expected to red-shift with increasing T, which is not the case here where a strong blue-shift in E_{PL} with increasing T is observed. Levcenko *et al.* saw very similar temperature-dependent PL behaviour in their CZTSSe films and concluded the deeper defect level E_{a2} is more probably a donor state in a p-type absorber[67].

Fig. 6 shows the room temperatutre excitation-dependent PL response of the In_2S_3-buffered film. A change in k value indicates a change in the main radiative recombination process from defect mediated at 6 K ($k < 1$, k = 0.80) to band-related at 295 K ($k > 1$, k = 1.13). Further evidence of a band-related transition is also demonstrated as there is no shift in the PL peak with in-

creasing excitation at room temperature. The inset in Fig. 6 shows room temperature PL spectra of the CdS-buffered and In_2S_3-buffered CZTSSe films. The PL peaks at 0.962 eV (CdS-buffered) and 0.944 eV (In_2S_3-buffered) are significantly red-shifted from their respective bandgaps at 1.144 eV determined from EQE measurements (see Supp. Fig. S3). As the CZTSSe absorber has *p*-type conductivity, a CB-acceptor transition is most likely responsible for the room temperature PL observations. Although the PL signal from the CdS-buffered film was too low to analyse accurately, it is reasonable to assume the same acceptor defect is also present in this film. The magnitude of the PL peak red-shift from room temperature bandgap is roughly equivalent to the activation energy of the acceptor defect, giving values of 182 meV and 200 meV for CdS-buffered and In_2S_3-buffered films, respectively. These activation energies are in agreement with our previous deep level transient spectroscopy (DLTS) study of CZTSSe solar cells[45]. Thus, it is speculated that radiative recombination in the buffered samples involves a band-to-impurity (BI) transition where recombination occurs between the CB and a deep acceptor defect.

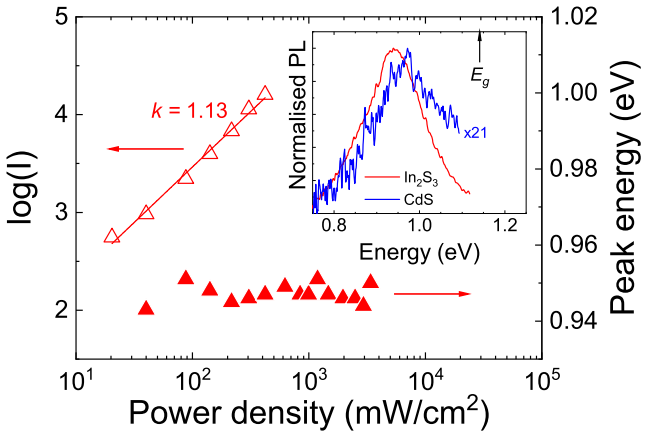

FIG. 6. Room temperature excitation-dependence of integrated PL intensity and PL peak position of the In_2S_3 based CZTSSe film with inset showing room temperature normalised PL spectra for CdS- and In_2S_3-buffered CZTSSe films with indicated bandgap of respective films.

Ab initio DFT calculations[13] reveal donor defects such as Zn_{Cu}, Sn_{Cu} antisites and Cu_i are shallow in nature whereas Sn-related acceptor defects such as V_{Sn}, Cu_{Sn} and Zn_{Sn} have formation energies in the range of the observed activation energies of acceptor defects found in the CZTSSe-based films studied here. Given the Cu-poor and Zn-rich growth conditions of the absorber films, it is reasonable to assume the donor and acceptor defects present are antisites Zn_{Cu} and Zn_{Sn}. Such conditions also promote higher concentrations of free hole carrier defect V_{Cu} and associated benign defect clusters [V_{Cu} + Zn_{Cu}] and [Zn_{Sn} + 2Zn_{Cu}] which are expected in all analysed CZTSSe-based films. Given the antisite defect Cd_{Cu} forms a shallow donor level with formation energy similar to Zn_{Cu}[58,69] and Cd diffusion into CZTSSe absorbers has been demonstrated experimentally[59,60], it is reasonable to assume the presence of Cd_{Cu} defects and [V_{Cu} + Cd_{Cu}] clusters in the surface region of the CdS-buffered CZTSSe film studied here. It would account for the increase in the degree of charge compensation determined from PL measurements for this thin film.

Based on all PL observations, radiative recombination in the CZTSSe-based films probably changes from QDAP or TI at low temperature to BI at higher temperatures involving the same deep acceptor defects, which are most likely Sn-related.

IV. Electrical device characterisation

The results of electrical device characterisation of CdS-buffered and In_2S_3-buffered CZTSSe solar cells are presented in Figs. 7 and 8 with device parameters shown in Table I. The *J-V* curves for the best performing devices measured in the dark and under 1-sun illumination are plotted in Fig. 7a. It is evident the In_2S_3-based device shows a clear drop in V_{oc} and suffers from poor shunt resistance R_{sh} ($\sim$25 Ωcm^2) compared to the CdS-based device ($\sim$106 Ωcm^2). As a consequence, the fill-factor (FF) is also reduced. The cause of the low shunt resistance is not immediately apparent as scanning electron microscopy (SEM) images reveal a conformal layer of In_2S_3 of thickness $\sim$70 nm following CBD (see Supp. Fig. S5). Also highlighted are the crossover points in the dark and illuminated *J-V* curves. Such a crossover can occur as a result of a voltage-dependent photocurrent due to a low built-in potential, the cause of which may be the presence of a Schottky barrier at the back contact or a depleted front layer[70]. In previous work[54], there was no evidence of a blocking barrier at the back contact, which suggests that the crossover issue may be due to the buffer-absorber interface. The log(J-J_{sc}) versus V plot for both types of device shows the superposition rule does not apply which is to be expected in non-ideal thin film solar cells and the photocurrent generated in both devices shows a slight voltage dependence, see Supp. Fig. S6.

To gain an insight into the reduced V_{oc}, capacitance-voltage (*C-V*) measurements were conducted at a frequency of 100 kHz. The *C-V* profile curves for CZTSSe devices with different buffers are presented in Fig. 7b. The carrier concentration N_A and depletion region width w_d for both devices at zero voltage bias are indicated on the plot. In terms of N_A, an increase in doping density of around one order of magnitude from 1.1 x 10^{16} cm^{-3} to 1.2 x 10^{17} cm^{-3} is observed for the In_2S_3-buffered compared to the CdS-buffered device. According to[72] the change in V_{oc} can be estimated by $\Delta V_{oc} = kT/q\ ln(N_{A1}/N_{A2})$, assuming a change only in the doping density of the absorbers being compared. The increase in doping density in the In_2S_3-based device should have an associated V_{oc} improvement of 61 mV. As V_{oc} can be detrimentally affected by high shunt conductance G_{sh}[62,73], this anomaly can be explained in terms of increased G_{sh} compared to the CdS-based device (G_{sh} (In_2S_3) = 39.3 mS/cm^2, G_{sh} (CdS) = 9.4 mS/cm^2). Similar carrier concentrations were observed in CZTSSe devices with In_2S_3 buffer layers and CZTSSe absorbers intentionally doped with In[30,62,74]. The elevated

Table I. Device parameters for the CZTSSe cells at room temperature. $R_{s,L}$, $R_{sh,L}$, n and J_0 are the series resistance, shunt resistance, ideality factor and reverse saturation current respectively, measured using the light *J-V* data (parameters were determined using methods described in[71]). E_g, N_A, w_d and L_d are the bandgap, apparent doping density, depletion region width and effective diffusion length, respectively

CZTSSe buffer	η (%)	FF (%)	V_{oc} (mV)	J_{sc} (mA/cm^2)	$R_{s,L}$ (Ω cm^2)	$R_{sh,L}$ (Ω cm^2)	A	J_0 (mA/cm^2)	E_g (eV)	N_A (cm^{-3})	w_d (nm)	L_d (nm)
CdS	3.2	42.6	255	26.1	1.64	106.3	2.0	4.9 x 10^{-2}	1.145	1.1 x 10^{16}	273	532
In_2S_3	2.3	35.3	220	27.3	2.27	25.4	1.6	1.4 x 10^{-3}	1.144	1.2 x 10^{17}	35	681

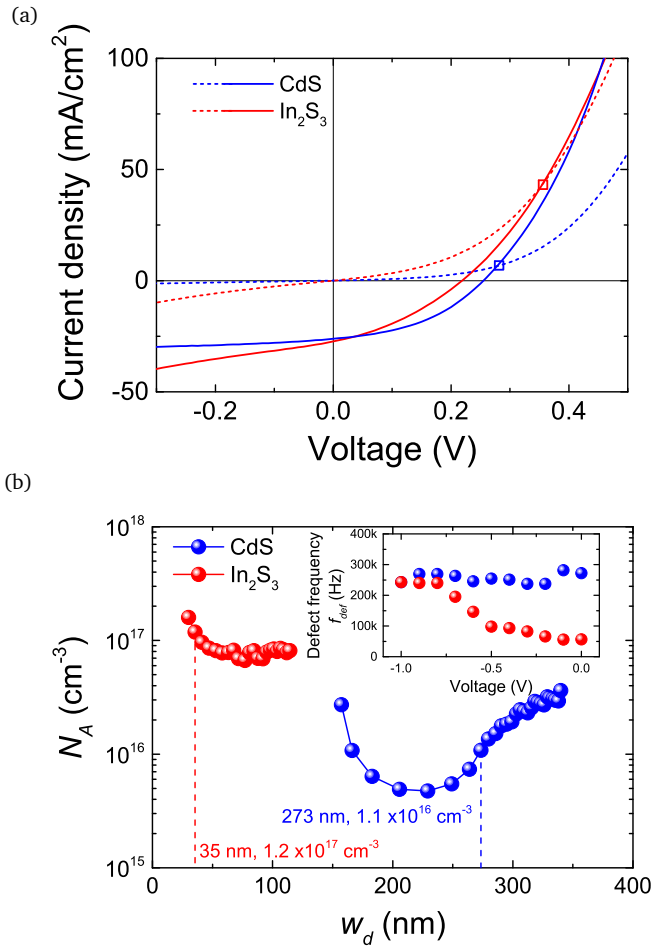

FIG. 7. (a) *J-V* curves of solar cells with CdS and In_2S_3 buffers measured in the dark (dashed lines) and under 1-Sun illumination (solid lines) with crossover points highlighted by □ and (b) *C-V* depth profiles with indicated w_d and N_A values at zero bias with inset showing voltage bias dependence of defect characteristic frequency f_{def}.

hole concentrations in these devices and ones studied here is mainly due to the substitution of Sn^{4+} with In^{3+}, facilitated by the similarity in their ionic radius[61]. The depletion region width w_d in the In_2S_3-buffered device is 35 nm, which is almost eight times shorter than that of the CdS-buffered device (w_d = 273 nm). As effective charge separation occurs in the depletion region in the absorber material of a solar cell, such a small w_d due to high hole concentration in CZTSSe adversely affects carrier collection. The effective carrier collection length L_{eff} is also related to the diffusion length of the minority carrier L_d and is roughly equal to w_d + L_d.

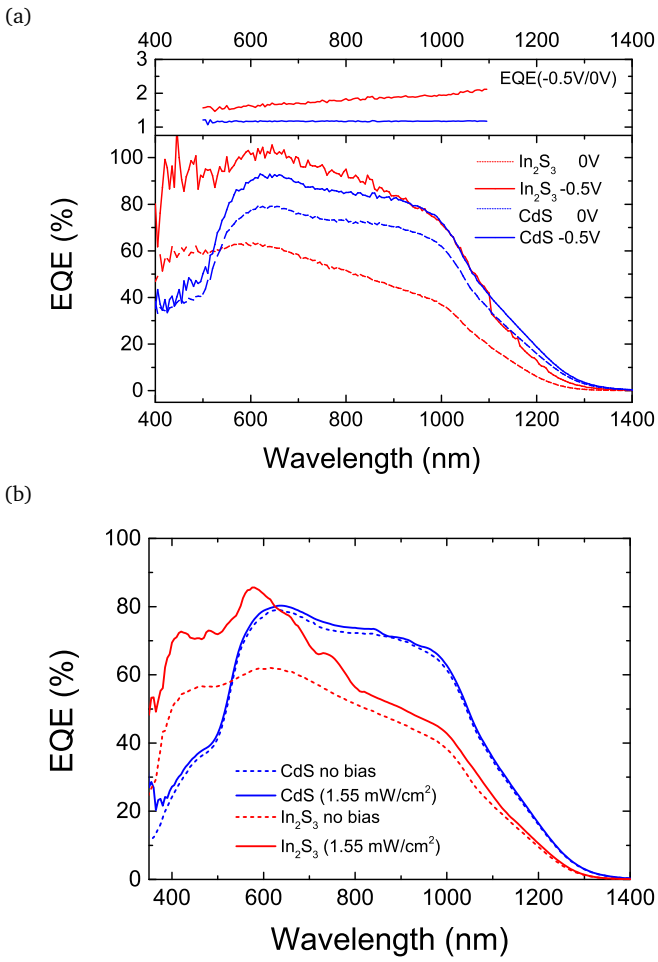

FIG. 8. (a) Reverse-bias EQE plots with EQE ratio -0.5/0 V of solar cells with CdS and In_2S_3 buffers and (b) light-biased EQE plots with CZTSSe solar cells under 1.55 mW/cm^2 illumination.

From analysis of absorption coefficient α and internal quantum efficiency (IQE) data (see Supp. Fig. S7) L_d values of 532 nm and 681 nm were extracted for CdS-buffered and In_2S_3-buffered CZTSSe solar cells, respectively. Due to the narrow space charge region in the In_2S_3-based device, the effective carrier collection length is significantly larger in the CdS-based device (L_{eff} (CdS) = 805 nm and L_{eff} (In_2S_3) = 716 nm). Reduced carrier collection from

longer wavelength photons in the In_2S_3-buffered solar cell is also evident in the EQE plots for both devices, see Fig. 8a. The unbiased EQE curves demonstrate the In_2S_3-buffered device is generally less efficient at carrier extraction than the CdS counterpart except in the sub 500 nm wavelength region where extraction is enhanced due to the higher bandgap and transparency of the In_2S_3 layer. The overall lower efficiency would suggest there is a greater barrier for electron transport in this device. The -0.5 V reverse biased EQE curves are also shown in Fig. 8a. By applying a reverse bias, photogenerated electrons can overcome the barrier leading to an enhancement in the EQE signal. The application of a reverse bias to the In_2S_3-buffered device results in a significant increase in EQE response. The ratio between unbiased and biased curves for the In_2S_3-based solar cell shows a gradual increase over the wavelength range 500 – 1100 nm indicating improved extraction of carriers at longer wavelengths. Reverse-biasing a solar cell increases the space charge region in the absorber and facilitates the carrier collection deeper into the absorber bulk. These observations are concurrent with lower effective carrier diffusion length in the In_2S_3-buffered device. Complimentary EQE measurements with and without white light bias (1.55 mW/cm^2) were performed, as shown in Fig. 8b. Considering the CZTSSe device with CdS buffer, the EQE response under light bias is slightly lower than that with light bias over the entire spectrum. Comparable results were observed in CZTS devices with CdS buffer layers[4,74]. The reduction in EQE was attributed to increased recombination in the space charge region. Conversely, the In_2S_3-buffered device exhibits a substantial increase in EQE over the wavelength region below 800 nm upon light bias application. It would appear that the In_2S_3/CZTSSe interface is photoactive and the increase in photoconductivity of the In_2S_3 layer increases the depletion region width leading to the observed higher collection efficiencies. To gain a better understanding of the buffer/absorber interface, capacitance-frequency (*C-f*) sweeps at different bias voltages were performed to evaluate interface and/or bulk defect characteristic frequencies f_{def}. *C-f* plots show a sharp decrease of capacitance at higher frequencies (see Supp. Fig. S8) and the inflection point in the capacitance curve corresponds to the defect characteristic frequency. The bias voltage dependence of f_{def} is illustrated in the inset of Fig. 7b. Varying the bias voltage changes the band bending near the buffer/absorber interface and adjusts the crossing point of the interface defect level and Fermi level. A shift of f_{def} with bias voltage indicates a predominance of interface defect states[75]. The characteristic defect frequency for the CdS-buffered device is roughly constant over the bias measurement range whereas the defect frequency for the In_2S_3 counterpart rises from ~60 kHz up to ~250 kHz. The presence of high concentrations of interface defects in the In_2S_3-based CZTSSe solar cell could account for the lower V_{oc} observed in the device.

With regard to In_2S_3/CZTSSe interface and device performance, SCAPS device simulations were performed to study the effect of varying interface defect concentrations, N_{int}. In these simulations, experimentally determined absorption data for CZTSSe, CdS and In_2S_3 thin films were used. The effects of donor-like CZTSSe/In_2S_3 interface defects were tested on Mo/CZTSSe/In_2S_3(CdS)/*i*-ZnO stacks. A summary of all material parameters is listed in Supp. Table S2. The simulation results in Fig. 9a show that a reduction in interface defect concentrations from 3.0 x10^{14} cm^{-3} to 0.1 x10^{14} cm^{-3} results in an overall increase in carrier collection over the whole wavelength spectrum with an enhanced extraction in the blue photon range (< 500 nm).

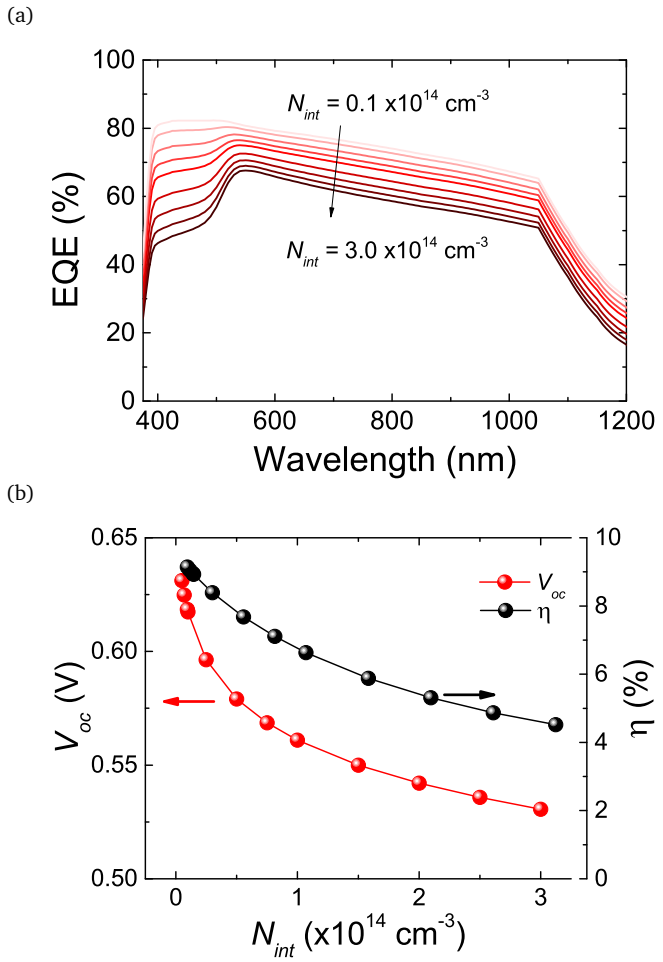

FIG. 9. SCAPS device modeling showing (a) EQE of In_2S_3-buffered CZTSSe solar cell with varying concentration of interface defects and (b) V_{oc} and η versus N_{int} plots.

Higher EQE in the 550 - 1050 nm range can be understood by increased photogeneration from an extended depletion region due to a reduction in interface defects. The simulated EQE curve at 3.0 x10^{14} cm^{-3} is in good agreement with experimental data (Figs. 8a and b). The simulation results suggest a reduction in interface states in the In_2S_3-buffered device would lead to J_{sc} improvement and consequent efficiency enhancement. Simulated *J-V* measurements were performed with increasing concentrations of interface defects and extracted V_{oc} and efficiency, η parameters are plotted as a function of N_{int} in Fig. 9b. It is apparent that a reduction in N_{int} leads to a significant increase in V_{oc} together with a marked improvement in device efficiency.

V. Conclusions

In summary, the interface properties between CdS and In_2S_3 buffer layers and kesterite CZTSSe absorber films fabricated from nanoparticle inks have been comprehensively investigated. XPS and IPES analysis revealed a preferential 'spike' conduction band offset of +0.39 eV at the In_2S_3/CZTSSe interface as opposed to a 'cliff' offset of -0.68 eV for the CdS/CZTSSe junction. PL studies of CdS- and In_2S_3-buffered CZTSSe thin films suggest the deposition of CdS induces chemical and electronic changes in the surface region of the CZTSSe film, probably caused by Cd diffusion into the absorber. As a consequence, the level of charge compensation is increased and free carrier concentration reduced. Mott-Schottky analysis shows In_2S_3 based solar cells have increased doping density, however the optimised conduction band alignment and elevated carrier concentration does not translate to improved performance in this type of device. Mott-Schottky analysis also indicated a prevalence of interface defects in the In_2S_3-buffered solar cells, accounting for the reduced V_{oc} observed in these devices. SCAPS device modeling of both types of CZTSSe solar cells showed a reduction in the concentration of interface defects led to an improvement in the efficiency of the In_2S_3 based devices due not only to increased V_{oc} but also enhanced J_{sc} compared to that with a CdS buffer. The results demonstrate the potential of In_2S_3 as a buffer material for CZTSSe absorbers providing that interface defects are mitigated using suitable absorber surface passivation or barrier layer deposition.

Supplementary Material

See supplementary material for additional information on the structural, optical and electronic properties of the studied CZTSSe thin films and solar cells.

Acknowledgments

The authors acknowledge support from the Engineering and Physical Sciences Research Council (EPSRC, Grant EP/N024389/1) and the North East Centre for Energy Materials (NECEM, Grant EP/R021503/1).

References

[1] K. Ito and T. Nakazawa, Japanese Journal of Applied Physics **27**, 2094 (1988).

[2] H. Katagiri, N. Sasaguchi, S. Hando, S. Hoshino, J. Ohashi, and T. Yokota, Solar Energy Materials and Solar Cells **49**, 407 (1997).

[3] N. Nakayama and K. Ito, Applied Surface Science **92**, 171 (1996).

[4] J. J. Scragg, P. J. Dale, L. M. Peter, G. Zoppi, and I. Forbes, physica status solidi (b) **245**, 1772 (2008).

[5] K. Moriya, K. Tanaka, and H. Uchiki, Japanese Journal of Applied Physics **44**, 715 (2005).

[6] K. Timmo, M. Altosaar, J. Raudoja, K. Muska, M. Pilvet, M. Kauk, T. Varema, M. Danilson, O. Volobujeva, and E. Mellikov, Solar Energy Materials and Solar Cells **94**, 1889 (2010).

[7] K. Tanaka, N. Moritake, and H. Uchiki, Solar Energy Materials and Solar Cells **91**, 1199 (2007).

[8] A. Darga, D. Mencaraglia, Z. Djebbour, A. Migan Dubois, J. Guillemoles, J. Connolly, O. Roussel, D. Lincot, B. Canava, and A. Etcheberry, Thin Solid Films **517**, 2550 (2009).

[9] T. K. Todorov, K. B. Reuter, and D. B. Mitzi, Advanced Materials **22**, E156 (2010).

[10] W. Wang, M. T. Winkler, O. Gunawan, T. Gokmen, T. K. Todorov, Y. Zhu, and D. B. Mitzi, Advanced Energy Materials **4**, 1301465 (2013).

[11] M. A. Green, Y. Hishikawa, E. D. Dunlop, D. H. Levi, J. Hohl-Ebinger, M. Yoshita, and A. W. Ho-Baillie, Progress in Photovoltaics: Research and Applications **27**, 3 (2018).

[12] P. Jackson, R. Wuerz, D. Hariskos, E. Lotter, W. Witte, and M. Powalla, Physica Status Solidi (RRL) - Rapid Research Letters **10**, 583 (2016).

[13] S. Chen, A. Walsh, X.-G. Gong, and S.-H. Wei, Advanced Materials **25**, 1522 (2013).

[14] T. Gokmen, O. Gunawan, T. K. Todorov, and D. B. Mitzi, Applied Physics Letters **103**, 103506 (2013).

[15] B. G. Mendis, M. D. Shannon, M. C. J. Goodman, J. D. Major, A. A. Taylor, D. P. Halliday, and K. Durose, Journal of Physics: Conference Series **471**, 012014 (2013).

[16] D. M. Bishop, B. McCandless, T. Gershon, M. A. Lloyd, R. Haight, and R. Birkmire, Journal of Applied Physics **121**, 065704 (2017).

[17] G. Rey, G. Larramona, S. Bourdais, C. Choné, B. Delatouche, A. Jacob, G. Dennler, and S. Siebentritt, Solar Energy Materials and Solar Cells **179**, 142 (2018).

[18] J. J. S. Scragg, J. K. Larsen, M. Kumar, C. Persson, J. Sendler, S. Siebentritt, and C. Platzer Björkman, Physica Status Solidi (b) **253**, 247 (2015).

[19] S. Bourdais, C. Choné, B. Delatouche, A. Jacob, G. Larramona, C. Moisan, A. Lafond, F. Donatini, G. Rey, and S. Siebentritt, Advanced Energy Materials **6**, 1502276 (2016).

[20] O. Gunawan, T. K. Todorov, and D. B. Mitzi, Applied Physics Letters **97**, 233506 (2010).

[21] D. A. R. Barkhouse, O. Gunawan, T. Gokmen, T. K. Todorov, and D. B. Mitzi, Progress in Photovoltaics: Research and Applications **20**, 6 (2011).

[22] A. Crovetto and O. Hansen, Solar Energy Materials and Solar Cells **169**, 177 (2017).

[23] T. Song, A. Kanevce, and J. R. Sites, Journal of Applied Physics **119**, 233104 (2016).

[24] R. Scheer, Journal of Applied Physics **105**, 104505 (2009).

[25] M. Bär, B.-A. Schubert, B. Marsen, R. G. Wilks, S. Pookpanratana, M. Blum, S. Krause, T. Unold, W. Yang, and L. e. a. Weinhardt, Applied Physics Letters **99**, 222105 (2011).

[26] S. Chen, A. Walsh, J.-H. Yang, X. G. Gong, L. Sun, P.-X. Yang, J.-H. Chu, and S.-H. Wei, Physical Review B **83**, 125201 (2011).

[27] M. Sandoval-Paz, M. Sotelo-Lerma, J. Valenzuela-Jáuregui, M. Flores-Acosta, and R. Ramiírez-Bon, Thin Solid Films **472**, 5 (2005).

[28] D. A. R. Barkhouse, R. Haight, N. Sakai, H. Hiroi, H. Sugimoto, and D. B. Mitzi, Applied Physics Letters **100**,

193904 (2012).
[29]F. Jiang, C. Ozaki, Gunawan, T. Harada, Z. Tang, T. Minemoto, Y. Nose, and S. Ikeda, Chemistry of Materials **28**, 3283 (2016).
[30]J. Kim, H. Hiroi, T. K. Todorov, O. Gunawan, M. Kuwahara, T. Gokmen, D. Nair, M. Hopstaken, B. Shin, and Y. S. e. a. Lee, Advanced Materials **26**, 7427 (2014).
[31]Y. Qu, G. Zoppi, R. W. Miles, and N. S. Beattie, Materials Research Express **1**, 045040 (2014).
[32]X. Xu, Y. Qu, V. Barrioz, G. Zoppi, and N. S. Beattie, RSC Advances **8**, 3470 (2018).
[33]Y. Qu, G. Zoppi, and N. S. Beattie, Solar Energy Materials and Solar Cells **158**, 130 (2016).
[34]Y. Qu, G. Zoppi, and N. S. Beattie, Progress in Photovoltaics: Research and Applications **24**, 836 (2016).
[35]D. Hariskos, M. Ruckh, U. Ruhle, T. Walter, H. Schock, J. Hedstrom, and L. Sstolt, Solar Energy Materials and Solar Cells **41-42**, 345 (1996).
[36]E. A. Kraut, R. W. Grant, J. R. Waldrop, and S. P. Kowalczyk, Physical Review Letters **44**, 1620 (1980).
[37]K. Sawangsri, P. Das, S. Supardan, I. Mitrovic, S. Hall, R. Mahapatra, A. Chakraborty, R. Treharne, J. Gibbon, and V. Dhanak, Microelectronic Engineering **178**, 178 (2017).
[38]J. T. Gibbon, L. Jones, J. W. Roberts, M. Althobaiti, P. R. Chalker, I. Z. Mitrovic, and V. R. Dhanak, AIP Advances **8**, 065011 (2018).
[39]H.-J. Chen, S.-W. Fu, S.-H. Wu, T.-C. Tsai, H.-T. Wu, and C.-F. Shih, Journal of Physics D: Applied Physics **49**, 335102 (2016).
[40]A. Santoni, F. Biccari, C. Malerba, M. Valentini, R. Chierchia, and A. Mittiga, Journal of Physics D: Applied Physics **46**, 175101 (2013).
[41]M. L. N. Palsgaard, A. Crovetto, T. Gunst, T. Markussen, O. Hansen, K. Stokbro, and M. Brandbyge, 2016 International Conference on Simulation of Semiconductor Processes and Devices (SISPAD) 10.1109/sispad.2016.7605225 (2016).
[42]T. Minemoto, T. Matsui, H. Takakura, Y. Hamakawa, T. Negami, Y. Hashimoto, T. Uenoyama, and M. Kitagawa, Solar Energy Materials and Solar Cells **67**, 83 (2001).
[43]M. Gloeckler and J. Sites, Thin Solid Films **480-481**, 241 (2005).
[44]Y. Cao, M. S. Denny, J. V. Caspar, W. E. Farneth, Q. Guo, A. S. Ionkin, L. K. Johnson, M. Lu, I. Malajovich, and D. Radu, Journal of the American Chemical Society **134**, 15644 (2012).
[45]S. Campbell, Y. Qu, J. D. Major, D. Lagarde, C. Labbé, P. Maiello, V. Barrioz, N. S. Beattie, and G. Zoppi, Journal of Physics D: Applied Physics **52**, 135102 (2019).
[46]A. P. Levanyuk and V. V. Osipov, Soviet Physics Uspekhi **24**, 187 (1981).
[47]J. Krustok, H. Collan, M. Yakushev, and K. Hjelt, Physica Scripta **T79**, 179 (1999).
[48]S. Siebentritt, N. Papathanasiou, and M. Lux-Steiner, Physica B: Condensed Matter **376-377**, 831 (2006).
[49]M. Yakushev, I. Forbes, A. Mudryi, M. Grossberg, J. Krustok, N. Beattie, M. Moynihan, A. Rockett, and R. Martin, Thin Solid Films **582**, 154 (2015).
[50]T. Schmidt, K. Lischka, and W. Zulehner, Physical Review B **45**, 8989 (1992).
[51]P. W. Yu, Journal of Applied Physics **48**, 5043 (1977).
[52]I. Dirnstorfer, M. Wagner, D. Hofmann, M. Lampert, F. Karg, and B. Meyer, Physica Status Solidi (a) **168**, 163 (1998).
[53]K. F. Tai, T. Gershon, O. Gunawan, and C. H. A. Huan, Journal of Applied Physics **117**, 235701 (2015).
[54]S. Campbell, Y. Qu, L. Bowen, P. Chapon, V. Barrioz, N. Beattie, and G. Zoppi, Solar Energy 10.1016/j.solener.2018.03.065 (2018).
[55]P. Y. Yu and M. Cardona, *Fundamentals of semiconductors* (Springer, 2005) p. 356.
[56]G. Rey, A. Redinger, J. Sendler, T. P. Weiss, M. Thevenin, M. Guennou, B. El Adib, and S. Siebentritt, Applied Physics Letters **105**, 112106 (2014).
[57]E. Zacks and A. Halperin, Phys. Rev. B **6**, 3072 (1972).
[58]Z.-K. Yuan, S. Chen, H. Xiang, X.-G. Gong, A. Walsh, J.-S. Park, I. Repins, and S.-H. Wei, Advanced Functional Materials **25**, 6733 (2015).
[59]C. Yan, J. Huang, K. Sun, S. Johnston, Y. Zhang, H. Sun, A. Pu, M. He, F. Liu, and K. e. a. Eder, Nature Energy **3**, 764 (2018).
[60]M. Sousa, A. da Cunha, J. Teixeira, J. Leitão, G. Otero-Irurueta, and M. Singh, Solar Energy Materials and Solar Cells **170**, 287 (2017).
[61]D.-H. Kuo and M. Tsega, Japanese Journal of Applied Physics **53**, 035801 (2014).
[62]Y. Pei, J. Guo, D. Kou, W. Zhou, Z. Zhou, Q. Tian, Y. Meng, and S. Wu, Solar Energy **148**, 157 (2017).
[63]M. Pilvet, M. Kauk-Kuusik, M. Altosaar, M. Grossberg, M. Danilson, K. Timmo, A. Mere, and V. Mikli, Thin Solid Films **582**, 180 (2015).
[64]M. Neuschitzer, M. E. Rodriguez, M. Guc, J. A. Marquez, S. Giraldo, I. Forbes, A. Perez-Rodriguez, and E. Saucedo, Journal of Materials Chemistry A **6**, 11759 (2018).
[65]S. Gao, Y. Zhang, J. Ao, X. Li, S. Qiao, Y. Wang, S. Lin, Z. Zhang, D. Wang, and Z. e. a. Zhou, Solar Energy Materials and Solar Cells **182**, 228 (2018).
[66]B. I. Shklovskij and A. L. Efros, *Electronic properties of doped semiconductors* (Springer, 1984) p. 297.
[67]S. Levcenko, J. Just, A. Redinger, G. Larramona, S. Bourdais, G. Dennler, A. Jacob, and T. Unold, Physical Review Applied **5**, 10.1103/physrevapplied.5.024004 (2016).
[68]J. Krustok, T. Raadik, R. Kaupmees, M. Grossberg, M. Kauk-Kuusik, K. Timmo, and A. Mere, Journal of Physics D: Applied Physics **52**, 285102 (2019).
[69]T. Maeda, S. Nakamura, and T. Wada, Japanese Journal of Applied Physics **51**, 10NC11 (2012).
[70]J. E. Moore, S. Dongaonkar, R. V. K. Chavali, M. A. Alam, and M. S. Lundstrom, IEEE Journal of Photovoltaics **4**, 1138 (2014).
[71]S. S. Hegedus and W. N. Shafarman, Progress in Photovoltaics: Research and Applications **12**, 155 (2004).
[72]U. Rau and H. Schock, Applied Physics A: Materials Science & Processing **69**, 131 (1999).
[73]R. E. Brandt, N. M. Mangan, J. V. Li, Y. S. Lee, and T. Buonassisi, Journal of Applied Physics **121**, 185301

(2017).
[74]C. Yan, F. Liu, K. Sun, N. Song, J. A. Stride, F. Zhou, X. Hao, and M. Green, Solar Energy Materials and Solar Cells **144**, 700 (2016).
[75]R. Herberholz, M. Igalson, and H. W. Schock, Journal of Applied Physics **83**, 318 (1998).
[76]A. Kanevce, I. Repins, and S.-H. Wei, Solar Energy Materials and Solar Cells **133**, 119 (2015).
[77]M. E. Erkan, V. Chawla, and M. A. Scarpulla, Journal of Applied Physics **119**, 194504 (2016).
[78]M. Hossain, P. Chelvanathan, M. Zaman, M. Karim, M. Alghoul, and N. Amin, Chalcogenide Letters **8**, 315 (2011).
[79]C. Persson, Journal of Applied Physics **107**, 053710 (2010).

Supplementary information

Table S1. A summary of the parameters used to obtain band offsets at the CdS/CZTSSe and In_2S_3/CZTSSe interfaces using the Kraut method[36]

Sample core level		$E_{cl}^{over,sub}$ (eV)	$\xi_{VBM}^{over,sub}$ (eV)	E_g (eV)	ΔE_v (eV)	ΔE_c (eV)
CdS (overlayer)	Cd $3d_{5/2}$	405.41	1.96	2.45	-	-
	S $2p_{3/2}$	161.82	1.96	2.45	-	-
CZTSSe (substrate)	Cu $2p_{3/2}$	932.47	0.39	1.15	-1.92	-0.62
	Zn $2p_{3/2}$	1021.96	0.39	1.15	-1.98	-0.68
	Sn $3d_{5/2}$	486.55	0.39	1.15	-2.02	-0.72
	Se $3d_{5/2}$	54.39	0.39	1.15	-1.98	-0.68
In_2S_3 (overlayer)	In $3d_{5/2}$	445.34	1.94	2.75	-	-
	S $2p_{3/2}$	161.82	1.94	2.75	-	-
CZTSSe (substrate)	Cu $2p_{3/2}$	932.47	0.39	1.15	-1.22	0.38
	Zn $2p_{3/2}$	1021.96	0.39	1.15	-1.12	0.48
	Sn $3d_{5/2}$	486.55	0.39	1.15	-1.33	0.27
	Se $3d_{5/2}$	54.39	0.39	1.15	-1.16	0.44

Table S2. Device simulation parameters, d: layer thickness, E_g: bandgap, χ: electron affinity, $\varepsilon/\varepsilon_0$: dielectric constant, ${m_e}^*/m_0$: effective mass, μ: carrier mobility, $N_{A/D}$: apparent doping density D:donor A:Acceptor, N_t:bulk defect density, E_t: defect energy level relative to VB, σ: capture cross section and N_{int}: interface defect concentration. Subscripts e and h are electron and hole, respectively.

Layer properties	CZTSSe	CdS	In_2S_3	i-ZnO
d (μm)	1.200	0.070	0.060	0.035
E_g (eV)	1.14[a]	2.42[a]	2.72[a]	3.37[b]
χ (eV)	4.6[c]	4.5[c]	4.7[d]	4.7[c]
$\varepsilon/\varepsilon_0$	8.5[e]	9.0[b]	13.5[d]	9.0[b]
${m_e}^*/m_0$	0.1[e]	0.25[b]	0.25[d]	0.275[b]
${m_h}^*/m_0$	0.32[e]	0.7[b]	0.7[d]	0.59[b]
μ_e (cm^2/Vs)	80[b]	160[b]	400[d]	200[b]
μ_h (cm^2/Vs)	25[b]	15[b]	210[d]	93[b]
$N_{A/D}$ (cm^{-3})	A: 5 x10^{16}[f]	D: 1 x10^{17}[b]	D: 1 x10^{18}	D: 1 x10^{18}[b]
Bulk defects (single level)				
N_t (cm^{-3})	A: 10^{14}[g]	D: 10^{17}[b]	D: 10^{18}	D: 10^{17}[b]
E_t (cm^{-3})	0.09[g]	0.10[b]	0.10	0.10[b]
N_t (cm^{-3})	A: 10^{14}[g]			
E_t (cm^{-3})	0.18[g]			
N_t (cm^{-3})	D: 10^{15}[b]			
E_t (cm^{-3})	0.63[b]			
σ_e (cm^2)	10^{-14}[b]	10^{-17}[b]	10^{-17}	10^{-12}[b]
σ_h (cm^2)	10^{-14}[b]	10^{-11}[b]	10^{-11}	10^{-15}[b]
Interface defects between CZTSSe and CdS/In_2S_3 (uniform distribution throughout interface)				
N_{int} (cm^{-3})		D: varied	D: varied	
σ_e (cm^2)		10^{-13}	10^{-13}	
σ_h (cm^2)		10^{-15}	10^{-15}	

[a] Experimentally determined from UV-VIS measurements
[b] Reference[76]
[c] Reference[77]
[d] Reference[78]
[e] Reference[79]
[f] Experimentally determined from *C-V* measurements
[g] Experimentally determined from PL measurements and DLTS in reference[45]

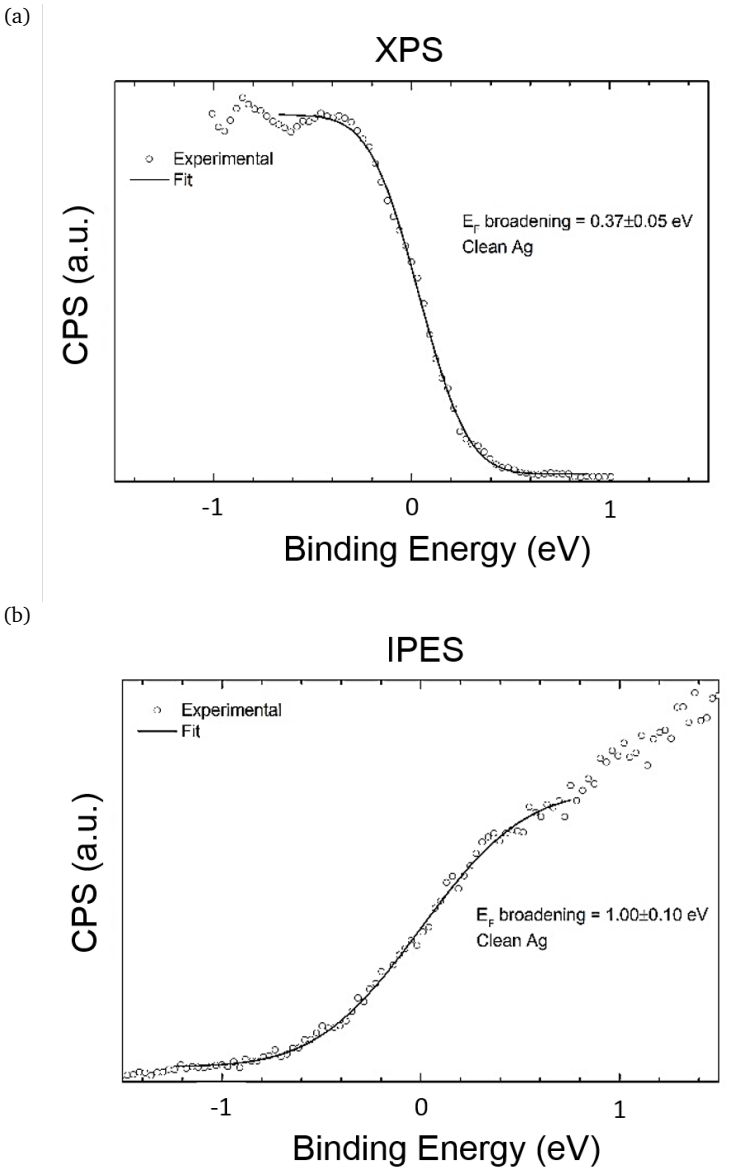

FIG. S1. Fermi level of a clean silver foil sample as measured by (a) XPS and (b) IPES.

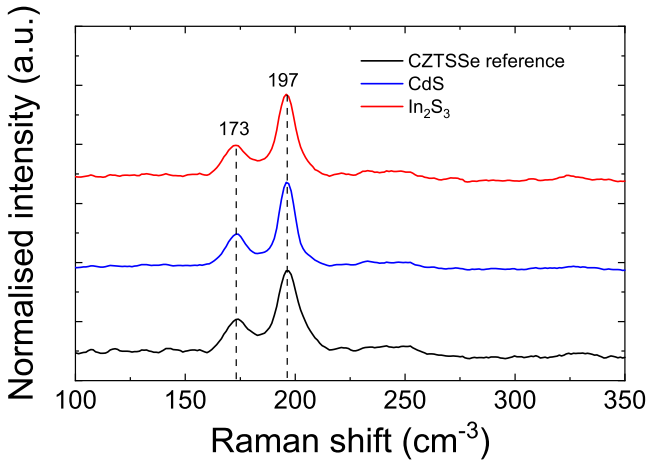

FIG. S2. Raman spectra of as-deposited reference, CdS- and In_2S_3-buffered CZTSSe absorber thin films.

(a)

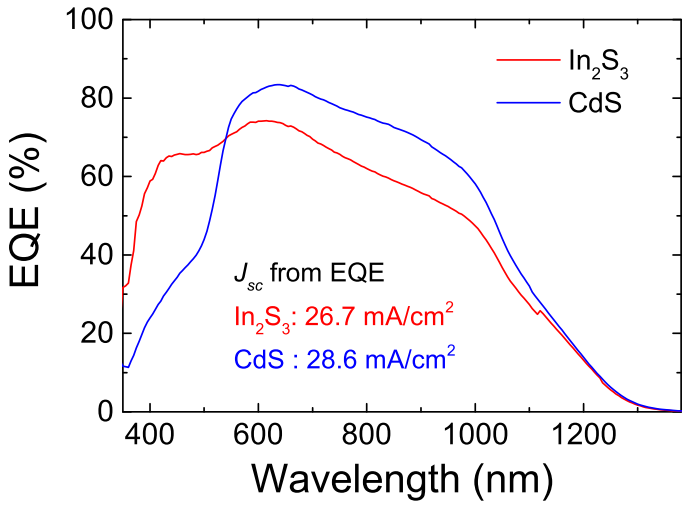

(b)

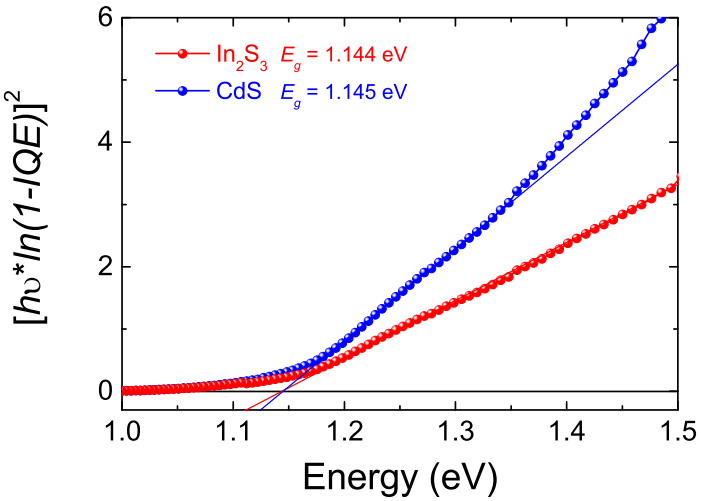

FIG. S3. (a) EQE plots for CdS- and In_2S_3-buffered CZTSSe devices and (b) bandgap determination for same devices from internal quantum efficiency (IQE) measurements.

(a)

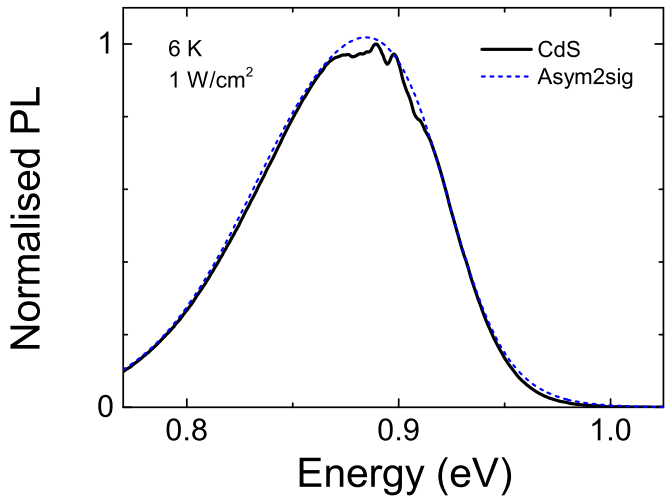

(b)

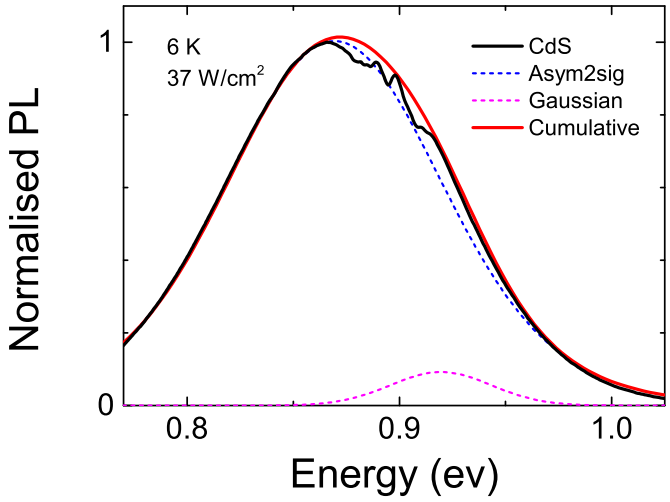

FIG. S4. (a) Asymmetric double sigmoidal peak fit at 0.885 eV of 6 K PL spectra from CdS based CZTSSe film under low excitation and (b) cumulative peak fitting of PL spectra from the same film under high excitation. Fitted with asymmetric double sigmoidal at 0.872 eV and gaussian at 0.920 eV which shows the emergence of another radiative transition. Note oscillations around 0.900 eV are due to water vapour absorption of light.

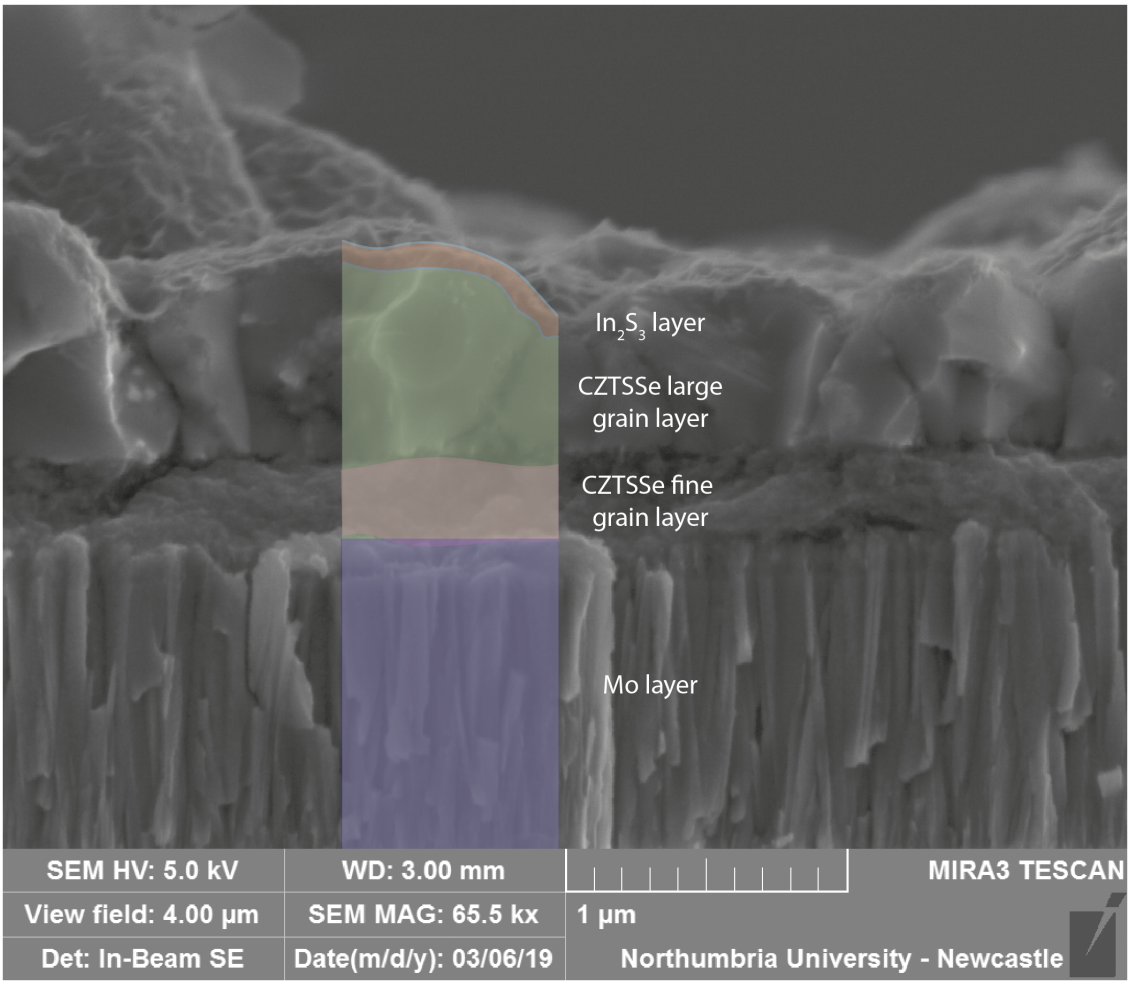

FIG. S5. Cross-sectional SEM image of In_2S_3-buffered CZTSSe thin film showing conformal coating of In_2S_3 layer.

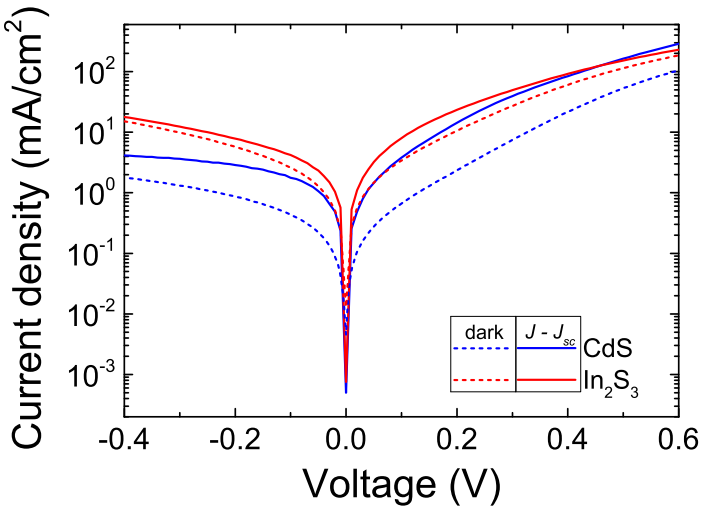

FIG. S6. *J-V* curves for CdS and In_2S_3 based CZTSSe devices with and without illumination.

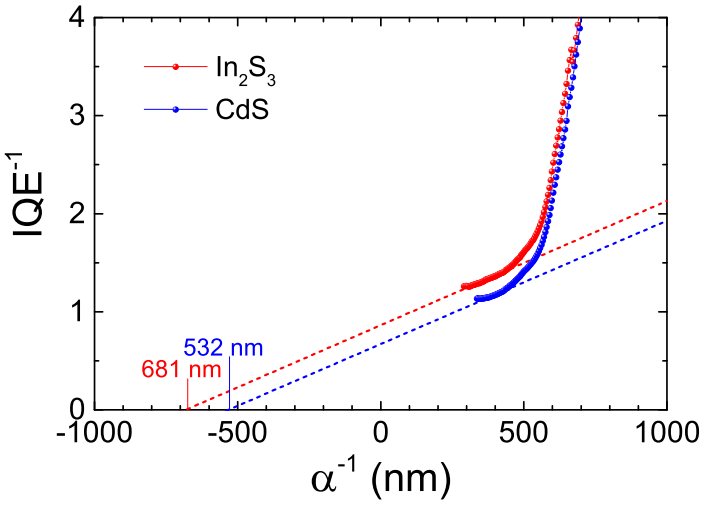

FIG. S7. Effective carrier diffusion length L_{eff} extracted from absorption coefficient/IQE data for CdS and In_2S_3 based devices.

(a)

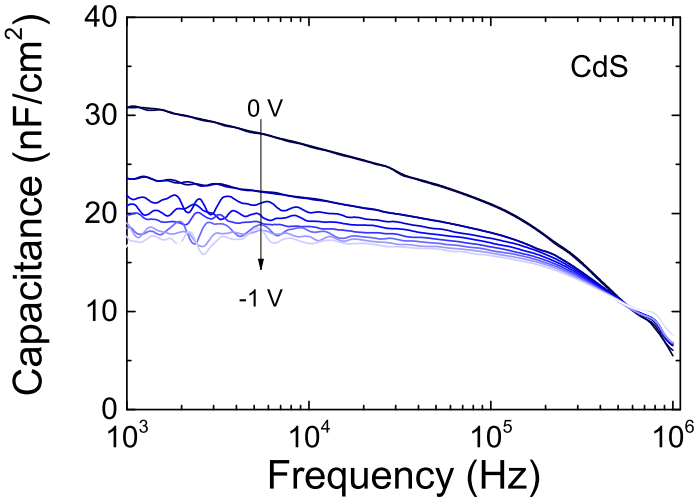

(b)

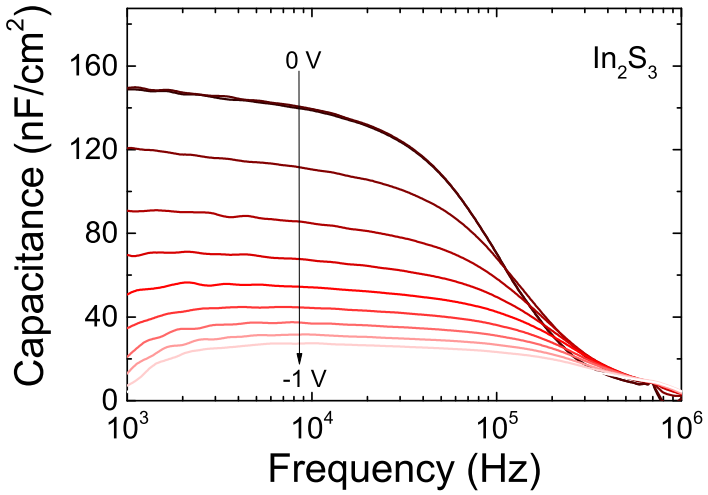

FIG. S8. *C-f* sweeps in reverse bias range 0 to -1 V of CZTSSe devices with (a) CdS and (b) In_2S_3 buffers.